Predicting Cone-in-Cone Blender Efficiencies from Key Material Properties

By: Dr. Kerry Johanson
Material Flow Solutions, Inc.

Abstract:

Blending of powders and granular materials is a critical unit operation in many industries, yet the ability to predict blending effectiveness lags well behind our ability to create new and novel blenders. As a result of this, production plants must rely on vendor blending tests conducted on small scale model blenders to determine if their specific material will work in the proposed blender design. Once these blending tests are conducted, engineers must then use past experience and conservative design practices to scale-up to full scale units at process flow rates.

The difficulty in predicting blending efficiencies arises from the fact that blending performance depends on basic material properties, blender geometry, blender flow rates, and blender operation parameters. These effects are convoluted during blending operation. Successful scale-up would require understanding how to separate the influence of these four effects. If this could be accomplished, blender performance could be determined by measuring simple material properties, predicting blender velocity profiles, and computing blender efficiencies from predicted velocity patterns. This method would allow separation of factors affecting blender performance and provide a means of reliable scale-up using simple material properties and specified blenders geometries.

This paper presents a methodology of predicting blender performance in simple in-bin blenders using easily measured material properties. It discusses blender optimization and determines the influence of gas pressure gradients on blender flow and operation. The specific blender analyzed is the cone-in-cone blender and the analysis suggests that blender performance depends on wall friction parameters for conditions where input concentration fluctuations occupy much of the blender volume. However, blending action appears to be independent of friction angle for conditions where there are many concentration fluctuations within a blender volume. The analysis also shows that gas pressure gradients can lead to stagnant region formation.

Key Words: Mass flow, Mixing, Residence Time Distributions, Powders, Solid Mechanics

Introduction

Acceptable blending of powder and granular materials requires three things. First, all material within the blender must be in motion during blender operation. Second, a distribution of material residence times must exist within the blender. Third, the blending shear and velocity profiles must result in mixing on a scale smaller than the size of the final product sample.

It is obvious from these three criteria that the specific motion in a given blender configuration determines the extent of blending caused by the process equipment. In fact, if flow profiles in any given blender were known, then they could be used to compute residence time distributions for the given blender configuration. These residence time distribution functions could then be used to evaluate blender performance.

Blending of powder material can be accomplished by imposing a velocity profile across a given piece of process equipment resulting in a distribution of residence times within the blender. For example, in well designed mechanical blenders all of the material in the blender is in motion during operation. In these blenders the velocity flow field is complex, resulting in particle flow paths that cross multiple times before exiting the blender. Since all particle flow paths do not travel the same distance before exiting the blender and individual particle velocities are different, the complex flow paths result in a residence time distribution function. Ideally, adjacent particles in a blender would have very different flow paths causing significant inter-particle mixing and produce wide residence time distribution functions. However, real blenders always shear material, often producing local zones which possess different trajectories and result in mixing down to the scale of local shear zones produced during the mixing processes. These local shear zones are caused by flow around paddles or screw flights and, when combined with the dynamic material trajectories, produce the overall blending in any given blender. In fact, the velocities in any given blender are due to shear or dynamic effects that move groups of particles around. Thus, to understand blending as a unit operation, one must be able to estimate the velocity profiles in both dynamic and shear flows. Every blender will have a combination of these velocity types. The main premise of this work is that material properties can be used along with specific blender geometries to predict blending velocity profiles. These velocity profiles can then be used to compute the expected blender residence time distribution functions and finally estimate the blender performance. This approach de-convolutes the effects of material properties, blender geometry, and blender operation parameters, making scale-up possible.

This approach is presented for the simple case of in-bin blenders such as the cone-in-cone. The dynamic material trajectories in this style blender occur only during blender filling as material free falls into the blender and distributes on the resulting pile. Most of the blending occurring in this type of blender results from shear velocity profiles caused by the specific blender geometry. The cone-in-cone blender will be used as an example to show how to de-convolute the effects of blender performance, material properties, blender geometry, and blender operation parameters and provide a methodology for blender scale-up. This blender will also be analyzed relative to the three criteria outlined above.

Cone-in-cone blenders

A cone-in-cone blender consists of a bin with a hopper that comprises two independent conical hopper sections as shown in Figure 1. One conical hopper section is inserted inside the other to form an interior conical hopper and an annular flow channel. Material flows through both the inner conical hopper and the annular region during blending operation. The vertical section

above the cone-in-cone is designed large enough to provide a mixing zone but is usually limited to a height equivalent to twice the diameter. Distribution chutes at the top of the blender spread the input flow stream across the blender cross section thus helping reduce possible segregation during blender filling. There is a conical hopper below the cone-in-cone section. The velocity profile across the cone-in-cone section combines with the velocity profile in the lower cone to yield a combined velocity profile responsible for axial blending in the in-bin blender. Material exiting this blender usually flows through some form of feeder to down stream process equipment. The cone-in-cone blender mixes well in the axial direction but provides only a small mixing capability in the radial direction. Hence, the feeder below the cone-in-cone provides radial mixing that is lacking from this style blender.

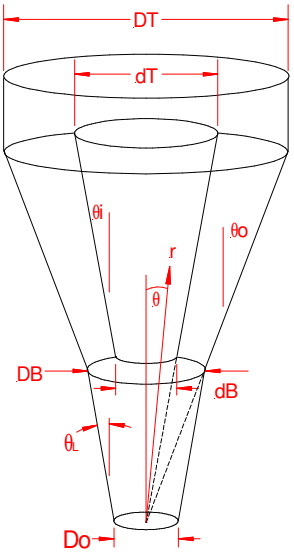

Figure 1. Schematic of typical cone-in-cone geometry

Mass Flow in Cone-in-cone blenders

The cone-in-cone hopper is a type of mass flow hopper. The interior cone and the lower cone are designed so the hopper slope angle is compatible with standard mass flow criteria. Simply stated, mass flow is a condition that produces significant material movement in the entire process equipment as material passes through or discharges from it (BMHB [1]). There are no stagnant regions in a mass flow bin. However, depending on the hopper shape and wall friction angle, a significant velocity profile can exist in a mass flow bin creating a residence time distribution. This property has been used successfully to create mass flow blenders (Ebert, et al [2], Johanson [3]).

The radial stress theory has been successfully used to compute the velocity in conical hoppers as well as to predict the mass flow limit. This theory will be extended to cone-in-cone hoppers as outlined below. These theories predict a relationship between the conical hopper half angle and the friction angle that is compatible with radial stress conditions. Figure 2 shows the calculated relationship between conical hopper angle and wall friction angle based on the radial stress theory (Jenike and Johanson [4], Nedderman [5]). It was shown that wall friction and hopper wall conditions that exceed the limiting line given in Figure 2 resulted in no flow along the walls or funnel flow.

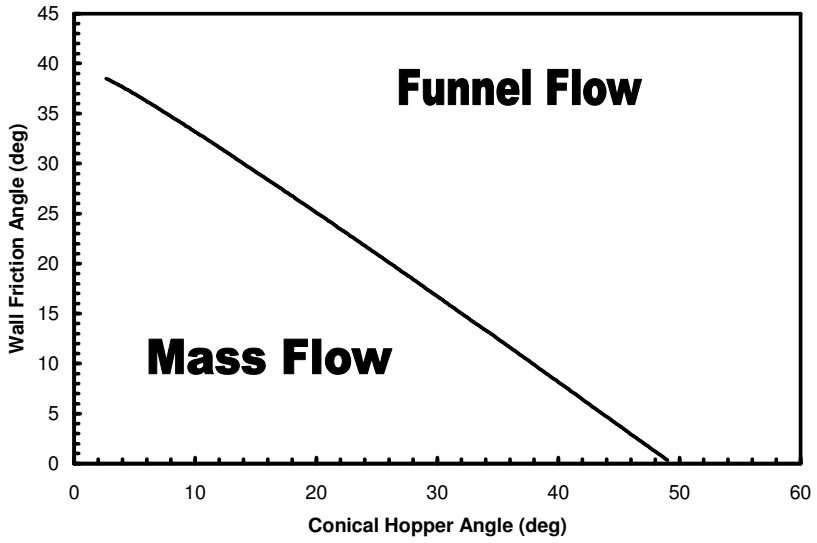

Figure 2. Typical mass flow funnel flow limit for effective internal friction angle of 50 degrees

The radial stress theory asserts that stress states within process equipment are compatible with radial stress fields and will produce mass flow in that process equipment. Non-radial stress states produce funnel flow behavior (stagnant region formation). In addition, the more frictional the wall surface, the steeper the velocity profile across the bin. Figure 3 shows the computed velocity profiles from the radial stress theory for a conical hopper with a hopper slope angle of 20 degrees measured from the vertical. This figure shows the increase in the steepness of the velocity profile as the wall friction angle increases. This radial stress theory will be discussed in more detail below.

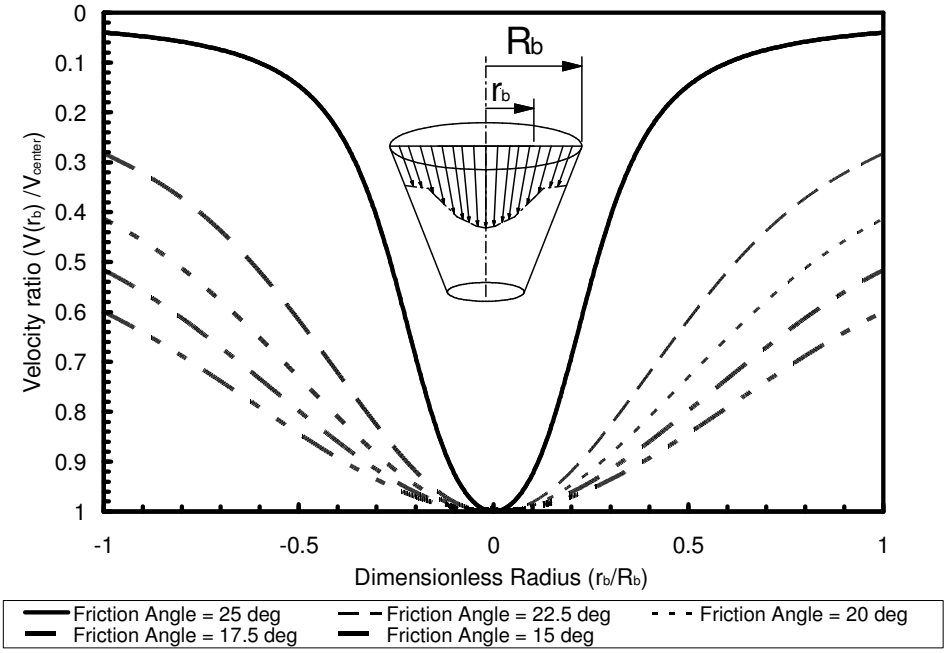

Figure 3. Conical velocity profiles in a 20 degree hopper with various friction angle along the bin wall

Computed radial velocities are well established for conical hoppers and could be extended to cone-in-cone geometries using the framework of the radial stress theory. Radial stress theory can be applied to cone-in-cone geometry since the two hoppers have a common apex. The overall objective of this work is to understand the relationship between blender velocities and the operational parameters. Therefore, the cone-in-cone radial theory will include external forces such as gas pressure gradients so the relationship between process flow and velocity profiles can be determined. The starting point for radial stress derivation is the equation of motion with the acceleration terms neglected. As a result, the radial stress theory applies to slow moving conditions in cone-in-cone geometries.

$$\nabla \cdot \underline{\underline{\tau}} = \gamma \underline{g} - \nabla P \qquad (1)$$

Spherical coordinates will simplify the numerical representation of equation 1 for the case of conical hoppers. The radial direction originates from the cone-in-cone apex resulting in equations 2 and 3 describing the relationship between the solid stress, bulk density, and gas pressure gradient.

$$\frac{1}{r^2}\cdot\frac{\partial\left(r^2\cdot\sigma_r\right)}{\partial r}+\frac{1}{r\cdot\sin(\theta)}\cdot\frac{\partial(\tau_{r\theta}\cdot\sin(\theta)}{\partial\theta}+ \frac{1}{r\cdot\sin(\theta)}\cdot\frac{\partial\tau_{r\phi}}{\partial\phi}-\frac{\sigma_\theta+\sigma_\phi}{r}=\gamma\cdot g_r-\frac{\partial P}{\partial r} \qquad (2)$$

$$\frac{1}{r^2}\cdot\frac{\partial(r^2\cdot\tau_{r\theta})}{\partial r}+\frac{1}{r\cdot\sin(\theta)}\cdot\frac{\partial(\sigma_\theta\cdot\sin(\theta))}{\partial\theta}+ \frac{1}{r\cdot\sin(\theta)}\cdot\frac{\partial(\tau_{\theta\phi})}{\partial\phi}+\frac{\tau_{r\theta}}{r}-\frac{\cot(\theta)}{r}\cdot\sigma_\phi=\gamma\cdot g_\theta-\frac{1}{r}\cdot\frac{\partial P}{\partial\theta} \qquad (3)$$

The Haar-Von Karman hypothesis can be used to eliminate some of the variables in equations 2 and 3. This hypothesis states that the normal stress (σ_ϕ) is either a major or minor principal stress. Normal hoop stress (σ_ϕ) equals major principal stress if the material flows through converging geometries, and equals the minor principal stress when flowing through diverging geometries. In either case, the shear stresses ($\tau_{r\phi}$) and ($\tau_{\theta\phi}$) acting on the ϕ–plane equal zero. This simplifies equations 2 and 3 to yield equations 4 and 5.

$$\frac{1}{r^2}\cdot\frac{\partial\left(r^2\cdot\sigma_r\right)}{\partial r}+\frac{1}{r\cdot\sin(\theta)}\cdot\frac{\partial(\tau_{r\theta}\cdot\sin(\theta)}{\partial\theta}-\frac{\sigma_\theta+\sigma_\phi}{r}=\gamma\cdot g_r-\frac{\partial P}{\partial r} \qquad (4)$$

$$\frac{1}{r^2}\cdot\frac{\partial(r^2\cdot\tau_{r\theta})}{\partial r}+\frac{1}{r\cdot\sin(\theta)}\cdot\frac{\partial(\sigma_\theta\cdot\sin(\theta))}{\partial\theta}+\frac{\tau_{r\theta}}{r}-\frac{\cot(\theta)}{r}\cdot\sigma_\phi=\gamma\cdot g_\theta-\frac{1}{r}\cdot\frac{\partial P}{\partial\theta} \qquad (5)$$

It is important to point out that there are four unknown stresses in the two equations above. Additional relationships between stress components are required to solve these two equations. The required relationship comes from the effective yield locus of the bulk solid (see Figure 4)

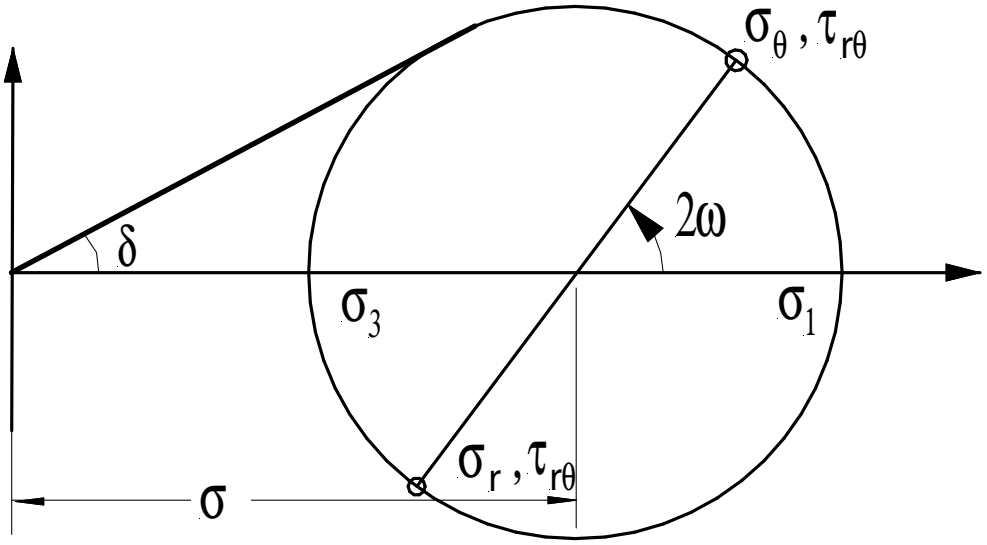

Figure 4. Limiting stress state definitions

Mohr circles are a graphical representation of the stress state acting on a bulk material. The effective yield locus is a line that is the envelope of the particular states of stress that represents a condition of continual deformation without volume change and is called the critical state of stress. This condition exists during steady flow in converging geometries. The relationship between stress tensor components can be derived using the definition of the effective yield locus and Mohr circle stress state geometry. This derived relationship provides the required closure equation for equations 4 and 5. The unknown stresses in these two equations can be represented as functions of the mean stress (σ) and the direction angle between major principal stress and the spherical coordinate system (ω). These relationships are given in equations 6 through 11.

$$\sigma_r = \sigma \cdot (1 - \sin(\delta) \cdot \cos(2 \cdot \omega)) \qquad (6)$$

$$\sigma_\theta = \sigma \cdot (1 + \sin(\delta) \cdot \cos(2 \cdot \omega)) \qquad (7)$$

$$\tau_{r\theta} = -\sigma \cdot \sin(\delta) \cdot \sin(2 \cdot \omega) \qquad (8)$$

$$\sigma_1 = \sigma \cdot (1 + \sin(\delta)) \qquad (9)$$

$$\sigma_3 = \sigma \cdot (1 - \sin(\delta)) \qquad (10)$$

$$\sigma_\phi = \sigma \cdot (1 + \sin(\delta)) \qquad (11)$$

The last equation required for the radial stress model comes from work done by Sokolovski [6]. He states that the mean solid stress near the apex of a wedge shaped section of a bulk material is proportional to the radial distance from the wedge apex to the point of interest. This yields equation 12 for the mean stress.

$$\sigma = \gamma \cdot g \cdot r \cdot s(\theta) \tag{12}$$

Substitution of equations 6 through 12 into equations 4 and 5 results in two equations in terms of the mean solids stress (σ) and the principal stress direction angle (ω). These derived equations assume that the effective angle of internal friction is constant and that the pressure gradients are only functions of radial position from the hopper apex.

$$\begin{bmatrix} -2 \cdot \sin(\delta) \cdot s \cdot \cos(2 \cdot \omega) \cdot \dfrac{d\omega}{d\theta} \\ -\sin(\delta) \cdot \sin(2 \cdot \omega) \cdot \dfrac{ds}{d\theta} \end{bmatrix} = \begin{bmatrix} \left(1 + \sin(2 \cdot \omega) \cdot \cot(\theta) + \right. \\ \left. \cos(2 \cdot \omega) \right) \cdot \sin(\delta) \cdot s + \\ (3 \cdot \sin(\delta) \cdot \cos(2 \cdot \omega) - 1) \cdot s - \\ (A_1 + \cos(\theta)) \end{bmatrix} \tag{13}$$

$$\begin{bmatrix} -2 \cdot \sin(2 \cdot \omega) \cdot \dfrac{d\omega}{d\theta} \\ +(\sin(\delta) \cdot \cos(2 \cdot \omega) + 1) \cdot \dfrac{ds}{d\theta} \end{bmatrix} = \begin{bmatrix} \left(1 - \cos(2 \cdot \omega) \cdot \cot(\theta) + \right. \\ \left. \sin(2 \cdot \omega) \right) \cdot \sin(\delta) \cdot s + \\ (3 \cdot \sin(\delta) \cdot \sin(2 \cdot \omega)) \cdot s + \\ (-A_2 + \sin(\theta)) \end{bmatrix} \tag{14}$$

$$A_1 = \frac{1}{\gamma \cdot g} \cdot \frac{\partial P}{\partial r} \tag{15}$$

$$A_2 = \frac{1}{\gamma \cdot g \cdot r} \cdot \frac{\partial P}{\partial \theta} \tag{16}$$

Equations 13 and 14 can be solved simultaneously to yield equations 17 and 18.

$$\frac{ds}{d\theta} = \frac{\begin{bmatrix} \sin(2 \cdot \omega) + \sin(\delta) \cdot \cot(\theta) \cdot \cos(2 \cdot \omega) - \\ \sin(\delta) \cdot \cot(\theta) - \sin(\delta) \cdot \sin(2 \cdot \omega) \end{bmatrix} \cdot s + \begin{bmatrix} -A_1 \cdot \cos(2 \cdot \omega) + \cos(2 \cdot \omega) \cdot \sin(\theta) + \\ A_2 \cdot \sin(2 \cdot \omega) + \sin(2 \cdot \omega) \cdot \cos(\theta) \end{bmatrix}}{\left(\cos(2 \cdot \omega) + \sin(\delta) \right)} \tag{17}$$

$$\frac{d\omega}{d\theta} = \frac{1}{2} \cdot \frac{\left[\begin{array}{l} \left[\begin{array}{l} \cos(\delta)^2 - \sin(\delta) \cdot \left(\begin{array}{l} \sin(2\cdot\omega)\cdot\cot(\theta) + \\ \cos(2\cdot\omega)+1 \end{array}\right) \cdot (\sin(\delta)+1) \end{array}\right] \cdot s + \\ \left[\begin{array}{l} A_1 \cdot (\sin(\delta)\cdot\cos(2\cdot\omega)+1) + \\ A_2 \cdot \sin(2\cdot\omega)\cdot\sin(\delta) \end{array}\right] + \\ \left(\begin{array}{l} \cos(2\cdot\omega)\cdot\cos(\theta) - \\ \sin(2\cdot\omega)\cdot\sin(\theta) \end{array}\right) \cdot \sin(\delta) + \cos(\theta) \end{array}\right]}{s \cdot \sin(\delta) \cdot \left(\cos(2\cdot\omega) + \sin(\delta)\right)} - 1 \qquad (18)$$

With the exception of the terms containing A1 and A2, these two equation are identical to the radial stress used by Jenike [7] [8], Johanson [4], and Nedderman [5]. The terms A1 and A2 include the gas pressure effects and can be used to estimate the influence of fluid pressures of the behavior of the bulk. It should be pointed out that the methodology used in this paper assumes the use of the traditional Mohr-Coulomb yield criteria. One could also apply a Drucker-Prager yield criteria as outlined in Jenike's work [9]. This will be a topic of further study.

Up to this point we have not made any distinction between the conical geometry and the annular geometry in the cone-in-cone. Consequently, equations 17 and 18 will apply to both geometries. However, the boundary condition for each geometry will be different. In the case of the conical geometry, the value of ω is known at the centerline of the hopper and at the hopper wall. In the case of the annular region, the value of ω is known at both the inner and outer hopper walls. The stress at the centerline of an axial symmetric conical hopper must be aligned with the principal stress direction. This implies that the angle between the coordinate axis and the direction of major principal stress (ω) equals zero.

$$\omega = 0 \quad at \quad \theta = 0 \qquad (19)$$

The other required boundary condition comes from the state of stress at the hopper wall. The stress condition at the wall must satisfy both the critical state of stress and the traditional columbic friction condition. Figure 5 shows a Mohr circle compatible with the critical state of stress. The line in Figure 5 indicates the columbic friction condition. Two intersection points satisfy these conditions. If the hopper converges, then the intersection at point A, representing the passive state of stress, applies. If the hopper diverges, then the active stress at intersection point B applies.

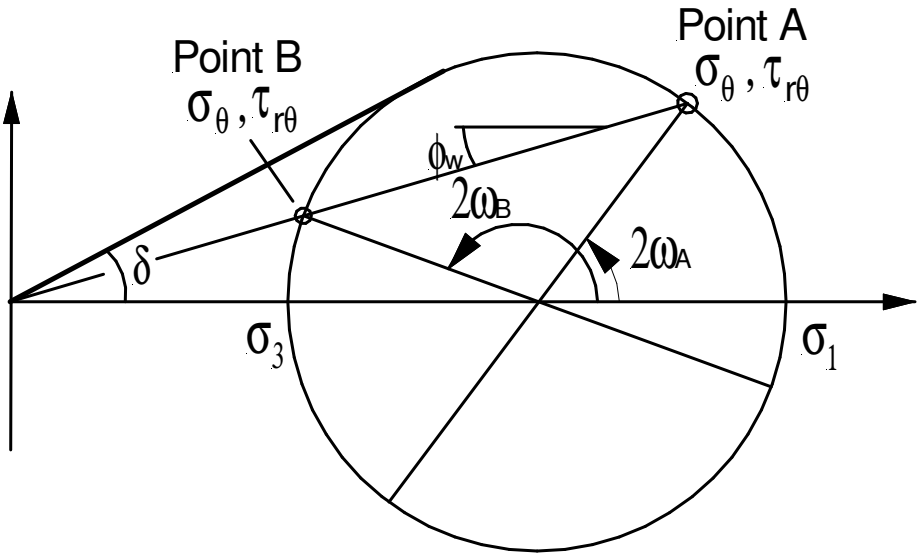

Figure 5. Two possible wall friction states for converging and diverging conical hopper geometries

The cone-in-cone is a converging geometry so the passive stress state applies. The concepts of passive and active stress states are borrowed from the discipline of soil mechanics. They arise from retaining wall terminology. In order to activate the stress state behind a retaining wall, the wall is pulled away from the material causing the stresses acting on the wall surface to be lower than the stresses acting vertically. Conversely, a passive state of stress results in wall stresses that are larger than the vertical stresses. The situation describing flow in a hopper is similar to a retaining wall, except the material moves and the wall is stationary. If the material flow direction causes material to pull away from the wall, then the active stress state applies, causing the wall stresses to be lower than the vertical stresses. This phenomenon occurs in diverging hoppers. Converging hoppers are then subject to passive stress states where the wall stresses are greater than the vertical stresses. The stress state represented by point A implies that the direction between the coordinate axis and the major principal stress is given by equation 20.

$$\omega = \frac{1}{2} \cdot \left(\phi_{we} + a\sin\left(\frac{\sin(\phi_{we})}{\sin(\delta)} \right) \right) \quad at \quad \theta = \theta_{iw} \qquad (20)$$

In non-aerated conditions, the wall friction angle is exclusively known and equations 17 and 18 can be integrated directly to produce a relationship between the principal stress direction angle (ω) and the hopper slope angle. However, the additional body forces caused by the gas pressure gradients near the hopper wall change the effective wall friction angle (i.e. the angle of slide against the wall). Gas pressure gradient is a body force term and is a vector quantity that can be added vectorally with the gravitational vector terms to produce a new vector component that acts at a direction (β) from the coordinate system (see Figure 6.). This implies that the total effective body force term acts in a direction other than the direction of gravitational pull. In effect the addition of gas pressure gradients causes the effective friction angle to act perpendicular to the β-direction in order to maintain equilibrium of forces. Consequently, the net effect of the gas

pressure gradient is to rotate the effective coordinate system relative to the gravitational direction. The new effective wall friction angle (ϕ_{we}) is given by equation 21.

$$\phi_{we} = \phi_w + \beta \qquad (21)$$

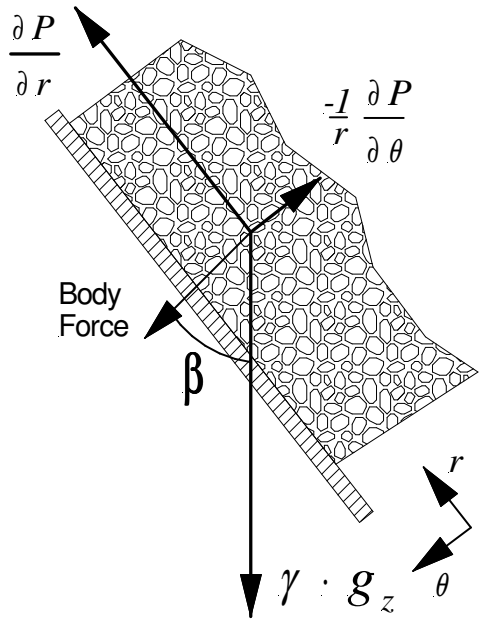

Figure. 6. Force balance at wall surface including gas pressure gradient terms

Angle (β) is a function of the pressure gradient in the radial and θ-directions. This leads to equation 22, describing the new effective wall friction angle in terms of the gas pressure gradient terms.

$$\phi_{we} = \phi_w + a\sin\left[\cos\left[\phi_w + a\tan\left[\frac{-\left[\frac{1}{r}\cdot\frac{\partial P}{\partial\theta}\right]_{wall}}{\left[\frac{\partial P}{\partial r}\right]_{wall}}\right]\right]\cdot\sqrt{\left(\left[\frac{1}{\gamma\cdot g}\cdot\frac{\partial P}{\partial r}\right]_{wall}\right)^2 + \left(\left[\frac{1}{r\cdot\gamma\cdot g}\cdot\frac{\partial P}{\partial\theta}\right]_{wall}\right)^2}\right] \qquad (22)$$

Equations 19 and 20 provide the required boundary conditions for standard conical hoppers. Equation 20 also applies to the outer wall in the annular region of the cone-in-cone geometry yielding the following equation for the outer wall boundary condition.

$$\omega = \frac{1}{2}\cdot\left(\phi_{we} + a\sin\left(\frac{\sin(\phi_{we}}{\sin(\delta)}\right)\right) \quad at \quad \theta = \theta_{ow} \qquad (23)$$

However, the inner wall in the annular region of the cone-in-cone requires different boundary conditions. Figure 7 shows the expected contours of major principal stress direction within the annular region. This figure implies that the direction of major principal stress is in the negative ω-direction along the inner cone wall. This suggests that the boundary condition along the outer surface of the inner cone wall is given by Equation 24:

$$\omega = -\frac{1}{2}\cdot\left(\phi_{we} + a\sin\left(\frac{\sin(\phi_{we})}{\sin(\delta)}\right)\right) \quad at \quad \theta = \theta_{iw} \tag{24}$$

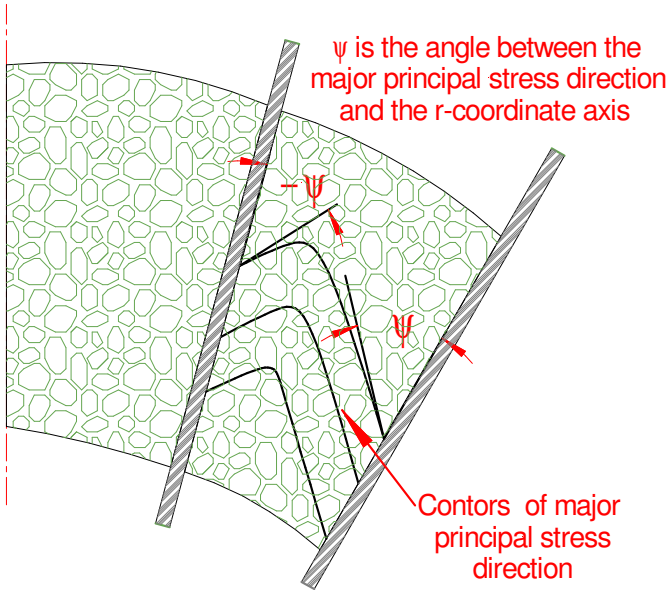

Figure 7. Direction of principal stress in annular region

Equations 17 and 18 can be integrated using boundary conditions given in equations 23 and 24 to produce radial stress solutions for annular geometries. Figure 8 shows some of the solutions for the case of a 10 degree inner cone. Careful examination of the solution space of these differential equations reveals no radial stress solutions to the right of the annular solution dotted line shown in Figure 8. This is similar to the result for the solution of radial stress field in standard conical hoppers. These standard conical hopper solutions also showed no radial solution to the right of the solid line shown in Figure 8. Experimental evidence suggests that this line is the limiting line between mass flow and funnel flow behavior for typical conical hoppers. It stands to reason that the limiting line for the annular geometry would also be the limit between mass flow and funnel flow behavior in the annular geometry. This figure reveals how a cone-in-cone hopper can be used to extend the mass flow limit to flatter hoppers for a given wall friction condition. Consider, for example, a material that has a friction angle of 33 degrees. The conical mass flow limit line shown in Figure 8 indicates that conical hoppers must be steeper than 10 degrees measured from the vertical to produce flow along hoppers walls. However, the solution for the same wall friction angle in an annular flow channel flow where the inner cone is 10 degrees is given by the dotted line in Figure 8. This figure implies that mass flow is possible if

the external hopper is about 22 degrees measured from the vertical. The net result is that this combination of hoppers shifts the limiting radial stress line towards flatter hoppers. Thus, the cone-in-cone geometry extends the mass flow limit to flatter outer cone angles. If material will flow in mass flow in a 10 degree conical hopper then the cone-in-cone hopper can be almost 22 degrees and still produce mass flow.

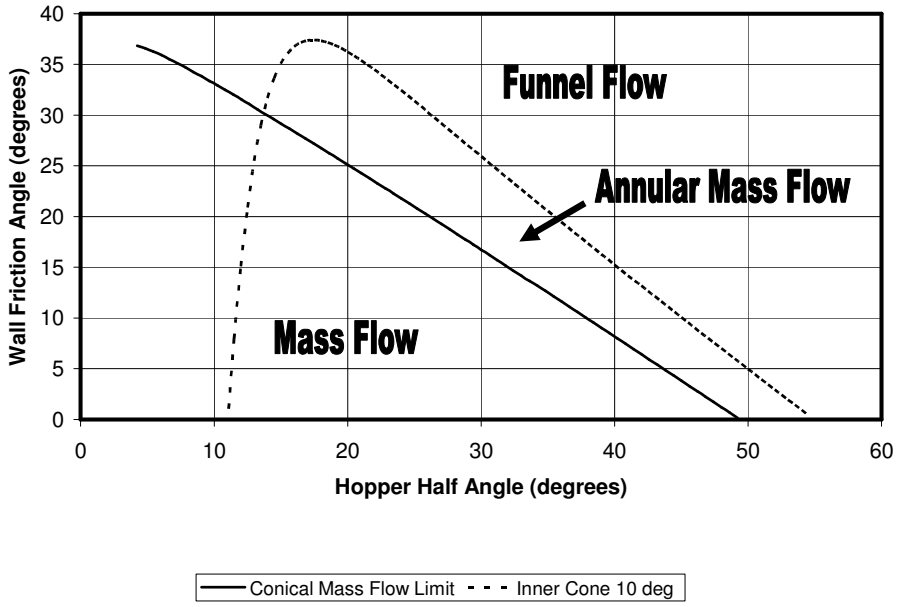

Figure 8. Mass flow limit for cone-in-cone hopper with inner cone of 10 degrees

This same analysis can be performed for various combinations of inner and outer conical hoppers. Figure 9 shows the predicted mass flow limit lines for several inner conical hopper configurations. Generally, if frictional characteristics of the inner and outer cone are the same and the inner hopper is designed for mass flow with a hopper angle of θc, then the outer hopper angle can be designed with a slope angle given by the balanced friction angle limit line found in Figure 9.

Conversely, if an existing conical hopper has a frictional condition that puts it in the funnel flow region, then Figure 9 could be used to determine the size and shape of the inner cone that would be required to cause flow along the walls. For example, consider the case of a 35^o conical hopper with a wall friction angle of 21^o. This cone would be in the funnel flow regime as indicated by the plus sign in Figure 9. However, if an inner cone with a 10^o slope was placed within the existing funnel flow hopper, then mass flow could be achieved.

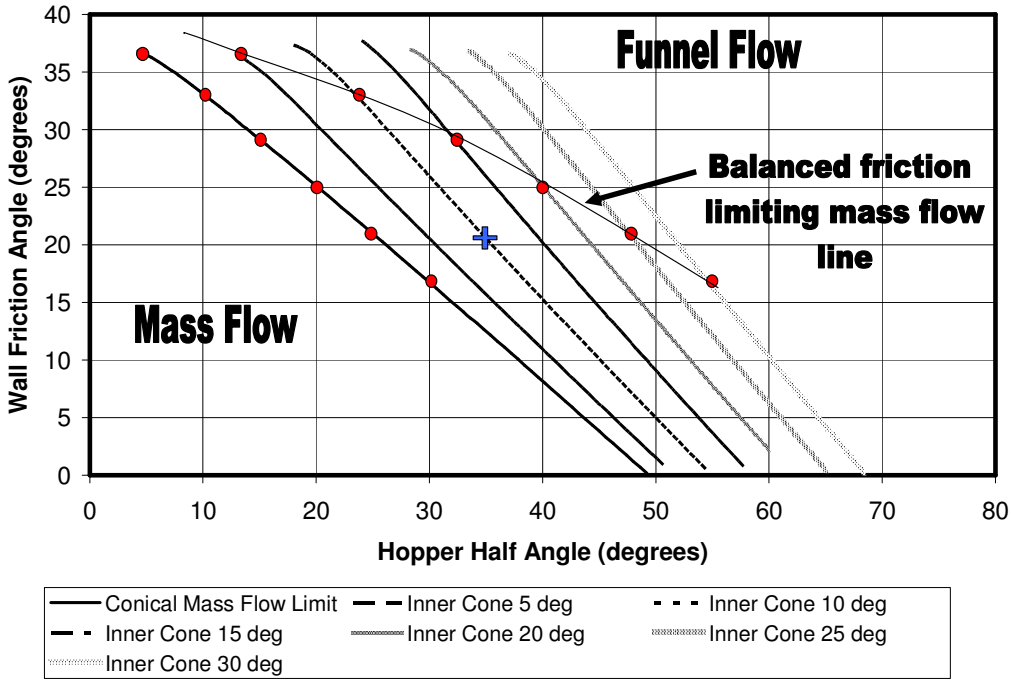

Figure 9. Balanced friction mass flow limiting line for cone-in-cone geometry (internal friction angle δ=50 deg)

The analysis above suggests that cone-in-cone geometries could be designed to produce mass flow during operation provided hopper walls are steep enough. Thus, designing the hopper angle in accordance with these limits will satisfy the first blender criteria that states that all of the mass within the blender must be in motion during blender operation. The above analysis determines the relationship between wall friction angle and the steepness of both the inner and outer hopper walls that will produce mass flow. Walls that are too frictional or too flat will result in flow patterns where at least some of the material in the blender is stagnant.

However, imposing just the concept of mass flow is not sufficient to guarantee significant blending. Traditional radial stress theory applied to standard conical hopers indicates that nearly uniform flow profiles can exist in hoppers where materials have low friction angles. It stands to reason that applying radial velocity patterns to the cone-in-cone geometries will also produce uniform flow patterns for low friction angle or steep hoppers. These nearly uniform velocity profiles will result in poor mixing. A method of computing velocity profiles in cone-in-cone geometries will be presented below.

It is important to note this mass flow criterion was determined solely from knowledge of basic material properties. Consequently, this analysis allows us to relate the general flow pattern to material properties. This is the first step in de-convoluting material properties and blender operation. The next step involves computing the expected velocity profile in the blender from just knowledge of material properties and blender geometry.

Velocity profiles in Cone-in-cone blenders

There are two ways velocity profiles can be affected in cone-in-cone hoppers. Since the cone-in-cone actually consists of two independent hopper sections, it is possible that these two hoppers sections have different average flow rates through them based on the areas of the top and bottom outlets. In fact, the cone-in-cone hopper dimensions can be specified to create a desired flow ratio between the inner cone and the annular region. Equation 25 shows how the inner cone outlet diameter can be chosen to specify the fraction (R) of global flow rate directed through the inner cone. This fraction is based on the ratio of flow areas at the top and bottom diameters of the cones. From a practical point of view, a typical cone-in-cone can achieve a maximum velocity ratio (R) between inner and outer cones of about five to one. Equation 25 can be used to estimate the inner cone diameter (d_B) required for a given velocity ratio ($R_{vel}=V_{inner}/V_{outer}$).

$$d_B = \frac{D_B}{\sqrt{\frac{\left(\frac{\sin(\theta_o)}{\sin(\theta_i)}\right)^2 - 1}{R_{vel}} + 1}} \qquad (25)$$

In addition to this global velocity pattern, the velocity across the hopper section will vary based on the wall friction conditions. This is a direct result of applying the radial stress and velocity theory to a cone-in-cone geometry. The cone-in-cone geometry with a common apex suggests that radial velocity profiles could also exist in the annular hopper region as well as the inner cone region. The radial velocity pattern is a function of the direction of principal stress in both the inner cone and annular hopper section. None of the assumptions regarding radial velocities are violated in annular conical flow so the standard radial velocity equations (Jenike and Johanson [4], Nedderman [5]) can be used to predict the velocities in annular conical geometries. The radial velocity in the inner cone can be approximated by equation 26 while the radial velocity in the annular region can be approximated by equation 27.

$$V(\theta) = V(0) \cdot \exp\left[-3 \cdot \int_0^{\theta iw} \tan(2 \cdot \omega) \cdot d\theta \right] \qquad (26)$$

$$V(\theta) = V(0) \cdot \exp\left[-3 \cdot \int_{\theta iw}^{\theta ow} \tan(2 \cdot \omega) \cdot d\theta \right] \qquad (27)$$

These equations yield an approximation to the velocity profile across both the inner and annular hopper sections that depend on wall friction angles, effective internal friction angles, and radial gas pressure gradients.

These velocities can be combined with the inner cone velocities to give the complete radial velocity pattern in a cone-in-cone hopper. Scaling factors can be applied to the inner and outer velocity profiles to adjust the flow ratio in the inner and outer geometries. Figure 10 shows two expected velocity patterns in a cone-in-cone hopper with a two-to-one velocity flow ratio (R_{vel})

from the inner to outer cones. These velocities are a function of the wall friction angle. Figure 10a predicts very flat velocity profiles with low wall friction angle materials. Figure 10b shows steeper velocity profiles with more frictional wall materials.

The flow profiles in Figure 10 assume that material exits the blender at the bottom of the cone-in-cone section. However, in good blenders there exists a conical hopper below the cone-in-cone section. The velocity profile in this conical hopper extension influences the overall blender velocity profile. The radial stress theory can be used to compute the expected velocity profile in the lower cone. This profile can be normalized to produce an average velocity equal to one. This normalized velocity profile can then be used as a multiplier on the cone-in-cone velocity to produce a new overall velocity profile that includes the effect of the lower conical hopper. Figure 11 shows how the velocity profiles above would be influenced by the conical section below the cone-in-cone.

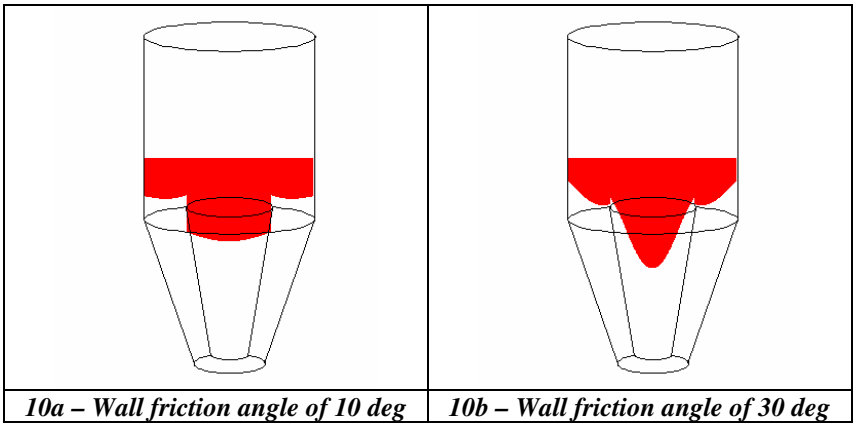

10a – Wall friction angle of 10 deg	*10b – Wall friction angle of 30 deg*

Figure 10. Velocity profiles in typical cone-in-cone geometries at two different friction conditions

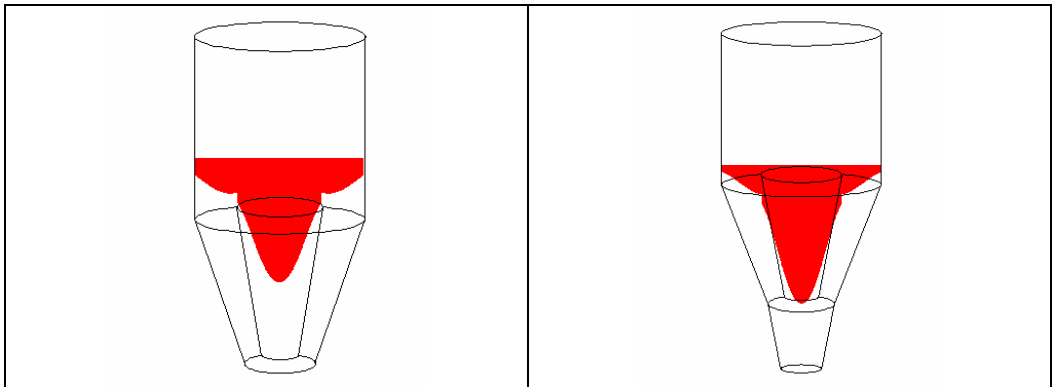

11a – Wall friction angle of 30 degrees; with a 3:1 flow rate ratio between inner and outer cones and no lower conical hopper placed below the blender.	*11b – Wall friction angle of 30 degrees; with 3:1 flow rate ratio between inner and outer cones and lower conical hopper.*

Figure 11. Velocity profiles showing the effect of the lower conical hopper on velocity profiles in cone-in-cone blenders

Residence time distribution functions in cone-in-cone blenders

Understanding blending in a cone-in-cone will require using these computed velocity profiles to determine the residence time distribution function (*E(t)*) for the blender and then using this residence time distribution function to compute the expected variance reduction factor in the blender. The standard way of evaluating continuous powder blender performance is to place a sudden impulse of markers in the blender, then operate the blender while maintaining the level in the blender and observe the discharge profile of markers leaving the blender. This exiting marker profile, when normalized to produce a total integrated concentration of one, is the residence time distribution function. The problem with this experimental analysis is that changing the material, adjusting the rate, or slight modifications to blender geometry requires a whole new blender test to develop the new residence time distribution function. Thus scale-up of blender performance is nearly impossible for most blenders. However, if the velocity profile is known, then it is a moderately simple task to numerically place a unit impulse in the cone-in-cone blender and integrate the flow field to compute the distribution of markers exiting the blender as a function of time.

In the cone-in-cone geometry, calculated velocity profiles do not cross each other and, consequently, can be integrated along flow stream lines to determine the time that a particle placed at the top of the blender will exit the blender outlet. Computing the exit times for a layer of particles placed at the top of the blender gives rise to a method of computing the residence time distribution function of the blender. The procedure for computing residence time in the blender from material properties is as follows.

The time required for one complete blender volume to pass through the blender is divided into small equal increments. This incremental time unit is then used to compute the thickness of a mathematical marker layer placed at the top of the blender. The thickness of this layer represents the average distance traveled for material at the top of the bin in one time increment. The cross sectional area at the top of the blender is divided into rings of equal area, creating regions of constant volume. These regions will be subject to radial flow streamline velocities. The position of any of the regions over time can be computed by multiplying the radial velocity by the incremental time and vectorally adding this value to the last marker volume position. The position of these individual marker volumes can be continually monitored to determine the time when they exit the blender. The number of volume elements exiting the blender divided by the total number of initial volume elements in the blender is an approximation of the blender residence time distribution. Perfect plug flow will result in all the marker volumes exiting the blender at the same time (after one blender volume discharge). Any deviation from this will produce a distribution in residence times and result in blending. Figure 12 shows a calculated residence time distribution function for a cone-in-cone hopper with a 10 degree inner cone and a 20 degree outer cone and a uniform velocity profile imposed below the cone-in-cone hopper. The relative flow rate variation between the inner and outer cone was two-to-one and the wall friction angle was 30 degrees measured from the horizontal. This figure also contains the velocity profile computed from this blender geometry. The initial marker layer comes from the center of the blender and exits the blender after only 0.5 blender volumes have passed through the system. The large peak is from the sudden change in the slope of the blender profile and exits the blender after about 1.25 bender volumes have passed through the system. It is

important to point out that this figure represents the residence time distribution in terms of the total amount of material passing through the blender instead of the elapsed time in the blender itself. In other words, the number of blender volumes (BV) passing through the system would be equal to the residence time ($t_{residence}$) multiplied by the average mass flow rate (Qs_{avg}) of the material in the blender and divided by the blender mass capacity ($Cap_{blender}$).

$$BV = t_{residence} \cdot \frac{Qs_{avg}}{Cap_{blender}} \tag{28}$$

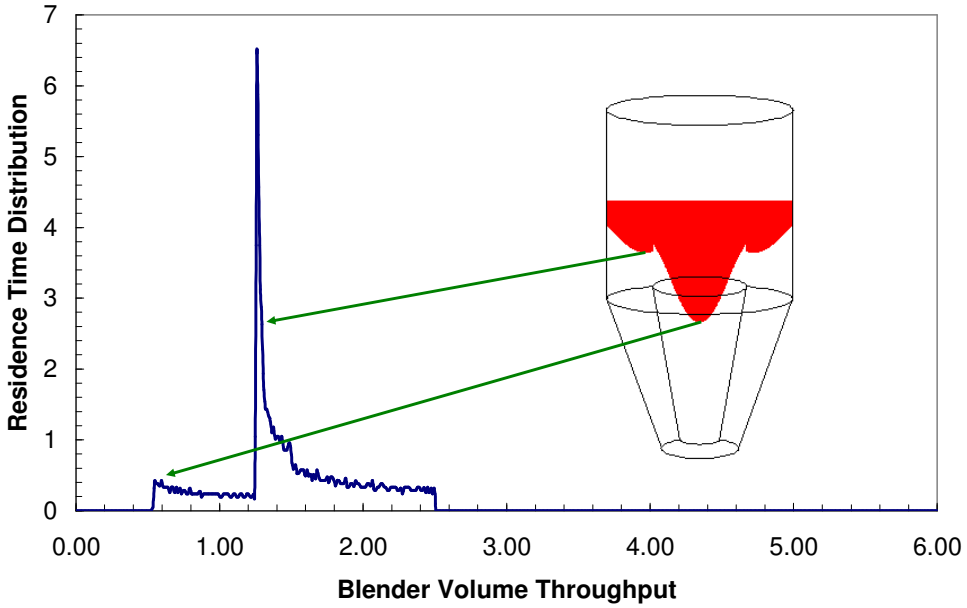

Figure 12. Residence time distribution function for cone-in-cone geometry shown in Figure 10b with wall friction angle of 30 degrees

Average residence time T_{avg} can be used to characterize blenders or other process equipment. However, two blenders may have the same average residence time but cause very different blending behaviors. In fact, it is possible to construct a bin where the material flows in nearly perfect uniform velocity mass flow. Residence time for this case would correspond to the time required for one blender volume to pass through the system. The distribution function in perfect mass flow would be a sharp concentration spike centered around one blender volume. This type of blender profile would not lead to blending and a uniform velocity mass flow bin would be a poor choice for a blender. A blender could also be constructed with an average residence time of one but distribute material over several bin volumes and result in good blending. Therefore, the width of the residence time distribution is more important in quantifying blending operation. It is the range of residence times in any blender that causes blending.

The residence time distribution function could be considered a blender finger print. With this distribution function, engineers can compute the expected concentration profiles for any input condition. Normally this residence distribution function is a measured quantity. The strength of this paper is the ability to compute the distribution function solely from measured material

properties for a given blender geometry. Once the residence time distribution function is known, any output concentration can be predicted by combining the input concentration function $C_{in}(t)$ and the residence time distribution function ($E(t)$) using the convolution integral given in Equation 29.

$$C_{out}(\tau) = \int_0^\infty C_{in}(\tau - t) \cdot E(t) \cdot dt \qquad (29)$$

Engineers can now compute the expected output concentration from a given cone-in-cone blender for any prescribed input concentration based only on a knowledge of basic material properties. For example, compare the input and output concentration profiles shown in Figure 13. The continuous blender operation smoothes the input concentration profile and produces a concentration profile with the same frequency but smaller variation exiting the blender. This result suggests that cone-in-cone blenders satisfy the second blending criteria which states that there must be significant residence time distributions within the blender for mixing to occur.

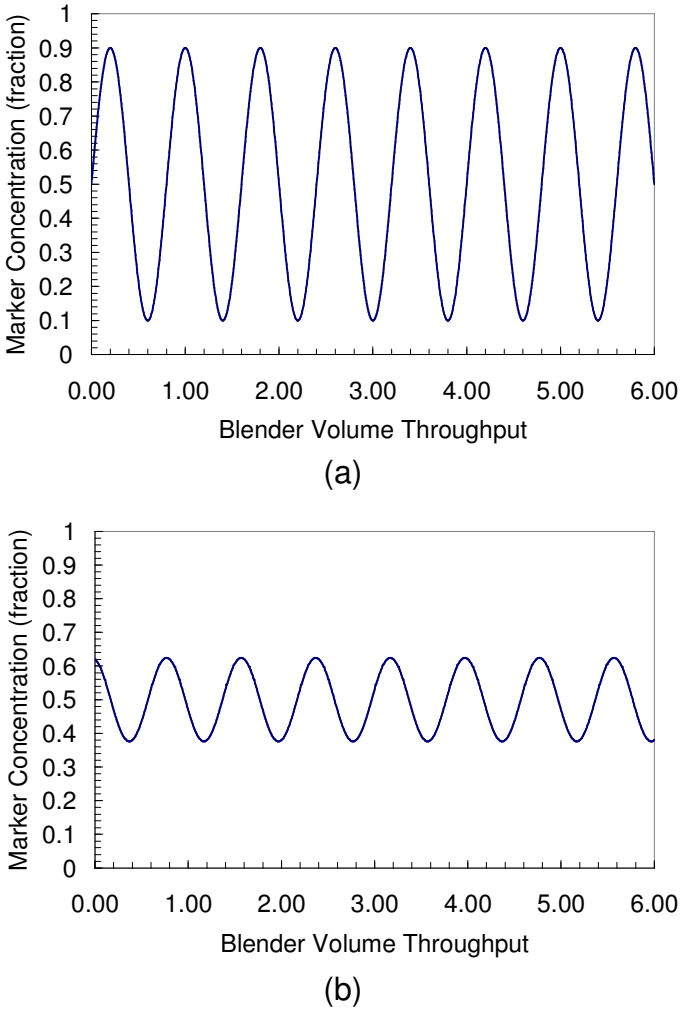

Figure 13. Input (a) and output (b) concentrations for blender with computed residence time distribution given in Figure 12 and input concentration period of 1.0

Figure 13 shows the expected reduction in output concentration fluctuation for the case where the period of concentration fluctuation extends over one complete bin volume. The number of fluctuations in a blender volume affects the degree of smoothing observed in the output concentration. This effect is shown in Figure 14 where the period of the input concentration function is less than one blender volume. This shorter period results in smaller output concentration fluctuations. One could compute the variance of the output concentration and divide that by the variance of the input concentration to provide a measure of blending effectiveness. This variance reduction factor can provide a means of ranking blender performance. Lower values of the variance reduction factor will result in better blending.

$$VR = \left(\frac{Sdev_{out}}{Sdev_{in}} \right)^2 \qquad (30)$$

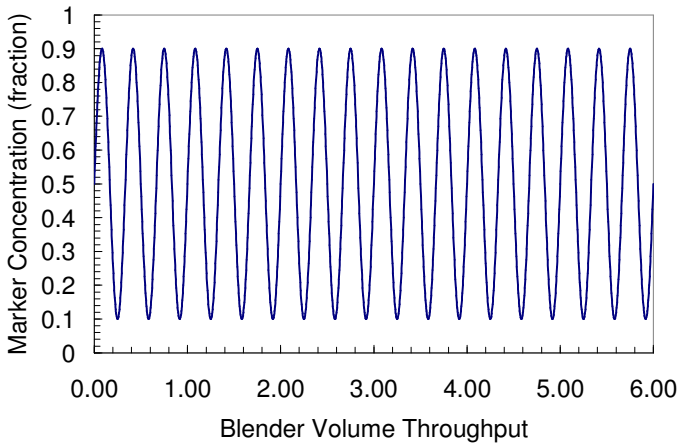

(a)

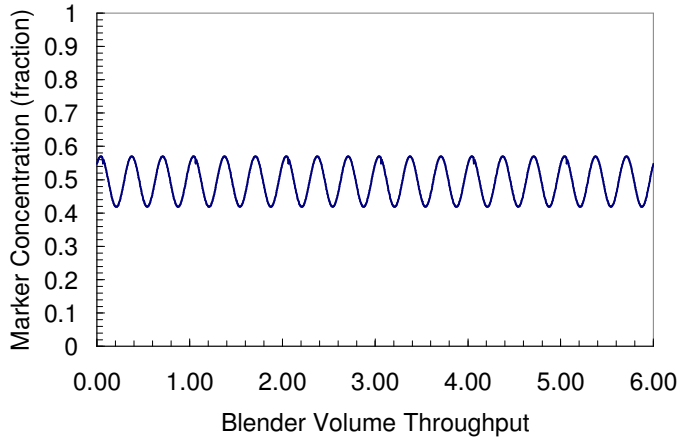

(b)

Figure 14. Input (a) and output (b) concentrations for blender with computed residence time distribution given in Figure 10 and input concentration period of 0.33

The example in Figure 13 above would result in a reduction factor of 0.086 while the example in Figure 14 would result in a reduction factor of 0.036, indicating better blending. It is important to point out that, in general, the greater the frequency or the shorter the period of the input concentration, the smaller the output concentration fluctuation. Since the above method allows calculation of the blender residence time distribution as a function of material properties and specific blender design constraints, it can be used for a parametric study of blend efficiencies based on flow properties and design constraints without having to measure blender distribution functions experimentally using expensive scale blender models.

For example, consider the case of a cone-in-cone blender with a 20 degree outer cone and a 10 degree inner cone. Consider also the effect of changing the input fluctuation frequency in two nearly identical blenders where the difference in these two blenders is the wall friction angle. Figure 15 shows the effect of blender variance reduction factors (*VR*) for two blenders where the number of input concentration fluctuation in one blender volume was varied. The number on the x-axis of this graph is the number of fluctuation periods of a sinusoidal varying concentration that enters the blender during the time it would take for one blender volume to pass through the system. The resulting variance reduction factor depends strongly on the number of fluctuations per blender volume. This figure clearly shows that, the larger the number of fluctuations per blender volume, the lower the variance reduction factor will be.

The results of this parametric study also suggest that the wall friction angle does not make a significant difference in blender effectiveness if the number of concentration input cycles is greater than about seven. However, there is a significant difference in blender efficiency in this blender when the number of input concentration cycles per blender volume is small. Thus, cone-in-cone blender operation becomes sensitive to material properties (i.e. wall friction) when attempting to blend fluctuations that occur over large blender volumes.

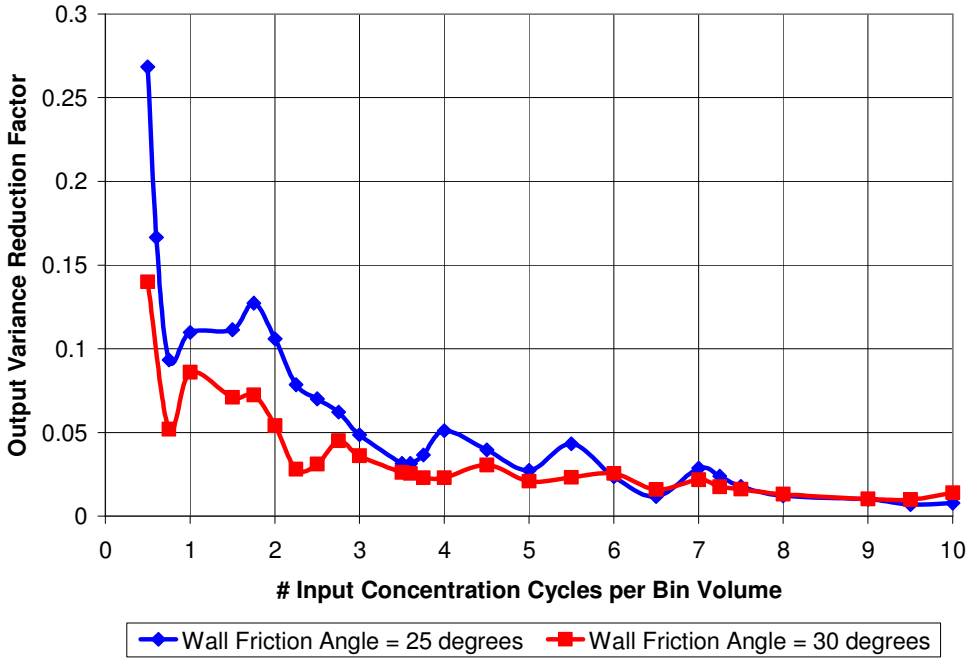

Figure 15. Variance reduction factors for identical blenders with a difference in wall friction angle

The influence of small changes in blender design can also be studied without conducting a blender test. Consider comparing two blenders where the wall friction angle is 30 degrees. Assume that the blender is designed with a 10 degree inner cone and a 20 degree outer cone. However, assume one blender discharges directly from the cone-in-cone section to the downstream process. Also assume that the inner cone diameter, for this blender, is designed with a two-to-one flow rate ratio. The other blender has a conical hopper below it that is imposing an additional blender velocity on the material and the inner cone diameter is increased to generate a three to one flow rate ratio between the inner cone and annular region. This second hopper configuration will result in a steeper velocity profile across the blender and should result in better blending. Figure 16 shows a comparison between the computed blender velocity profiles for these two blenders. The blender with the higher flow rate ratio and lower conical hopper has a centerline velocity that is 15 times greater than the velocity at the side wall. The blender with the two-to-one flow rate ratio between the inner and outer cones has a velocity that is only 4.6 times greater than the side wall velocity.

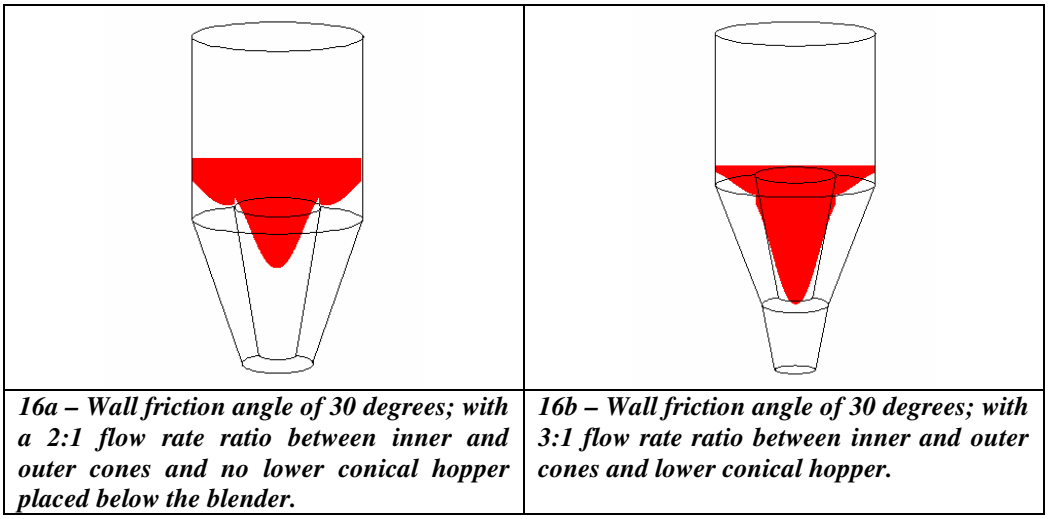

16a – Wall friction angle of 30 degrees; with a 2:1 flow rate ratio between inner and outer cones and no lower conical hopper placed below the blender.	***16b – Wall friction angle of 30 degrees; with 3:1 flow rate ratio between inner and outer cones and lower conical hopper.***

Figure 16. Velocity profiles showing the effect of the lower conical hopper on velocity profiles and flow rate ratio in cone-in-cone blenders

The variance reduction ratio for these two blenders can be computed and compared for a variety of period input concentration fluctuations. Figure 17 shows these results. The steeper velocity profile shows a significant decrease in the variance reduction factor for blending. However, for the case of a periodic input concentration there also exists a complex relationship between the input concentration frequency and the blender variance reduction factor. There appear to be zones of input concentration fluctuation frequencies that will result in low variance reduction factors. This effect may be due to the periodic nature of the input fluctuation and may not exist, or at least be reduced, for random concentration fluctuations. It is clear from this Figure that one of the primary variables influencing blending is the flow rate ratio between inner and outer cones. In general, the greater this ratio is, the better the blending will be. Intuitively, this makes sense. The greater the flow rate ratio between the inner and outer cones, the more distributed the layers become in the axial direction. Hence, blending is better.

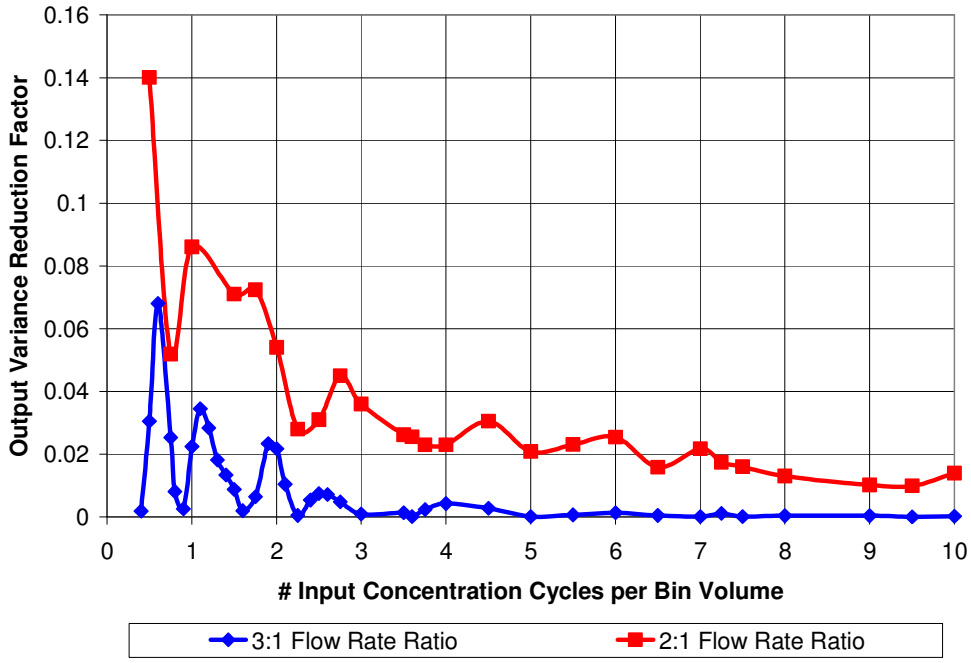

Figure 17. Variance reduction factors for blenders with differences in the flow rate ratio showing a decrease in blender variance reduction with larger flow rate ratios

This analysis also suggests that the optimal blender configuration will be one where the blending velocity profile is continuous and where the velocity in the center of the bin is an order of magnitude faster than the velocity at the blender wall. This type of velocity profile can only be accomplished by using a conical hopper in conjunction with a cone-in-cone hopper section. The strength of the analysis presented in this paper is the ability to make small modification to the blender design based on knowledge of the basic materials properties. Blender optimization can then be carried out without extensive and expensive pilot scale blender tests. Of course, prudence suggests that pilot scale testing should not be completely eliminated. However, the analyses suggest a method of at least reducing the pilot scale trials to achieve optimal blender design. Much of this design process can be accomplished numerically and then a small scale pilot unit constructed based of the optimal blender design. This design methodology should help engineers intelligently select or design a cone-in-cone blender to work with their particular materials.

Comparison to measured residence time distribution functions

A small scale cone-in-cone blender was constructed. The top diameter was 30.5 cm. The hopper section consisted of a 10 degree inner cone and a 20 degree outer cone that connected on to a 10.1 cm diameter conical hopper with a hopper slope of 10 degrees. The inner cone in the blender section was designed to produce a flow rate ratio of three to one. The wall friction angle against the hopper wall surface was 30 degrees. This blender configuration is similar to the configuration producing the velocity profile shown in Figure 16b. The analysis outlined above was carried out to compute the residence time distribution function for this blender configuration. The fraction of total markers passing through the blender outlet as a function of

time is defined as the accumulated residence time distribution function (F(t)) for this scale blender and is shown in Figure 18 along with a measured cumulative residence time distribution profile for this blender configuration. The initial marker appearance is the same for these two distributions. In addition, the residence time distributions end after the same volume input through the blenders. Agreement of these starting and ending points for the residence time distribution functions imply that the theory outlined above accurately captures the relationship between the centerline velocity and the velocity at the bin wall. However, the discrepancy between the measured and computed cumulative distribution functions indicate that the actual velocity profile does deviate somewhat from the computed profile.

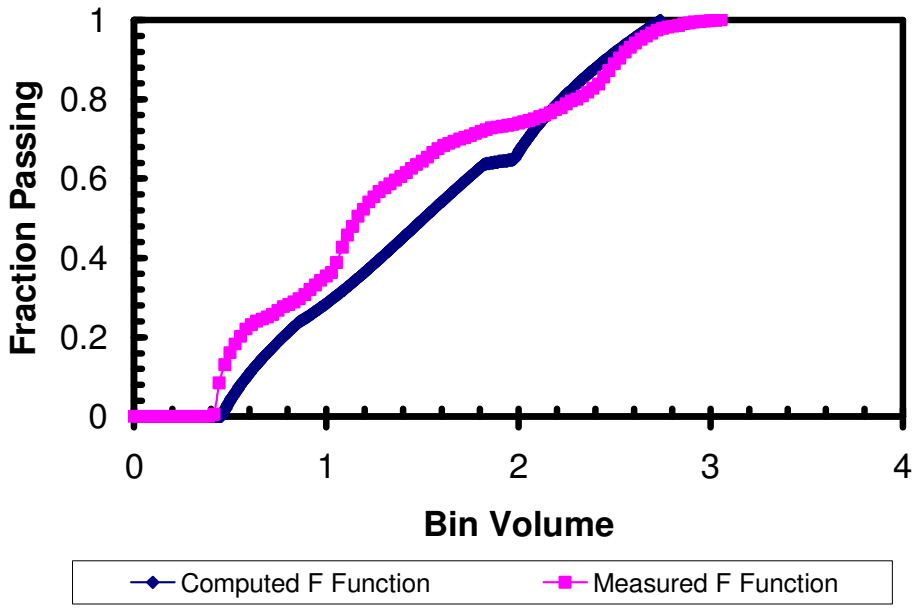

Figure 18. Cumulative residence time distribution function showing the cumulated fraction of markers exiting a model blender due to a unit impulse of markers

The differences between these distribution functions can be better seen when plotted as instantaneous residence time distribution functions (*E(t)*) as shown in Figure 19. The measured initial peak is larger than the calculated peak and there is a peak near one bin volume that does not match the calculated profile. Careful observation of the measure data may help explain these discrepancies. During the testing it was observed that the flow profile across the hopper was not completely symmetric and flow was slightly faster on one side of the hopper than the other. This non-symmetric flow profile could explain the spurious peak around 1.0 bin volume and the noticeable lack of markers around 1.8 bin volumes. The likely cause for this non-symmetric flow is an off-center conical insert. The relative flow between the inner and outer hoppers can be determined by the ratio of bin diameters. However, if the insert is positioned slightly off-center the local velocity on one side of the bin would speed up based on the increased gap between the inner and outer cones while the flow on the opposite inside would decrease due to the smaller gap between the inner and outer cones. The lack of dimensional tolerance could then account for the discrepancies in these two residence time distribution functions.

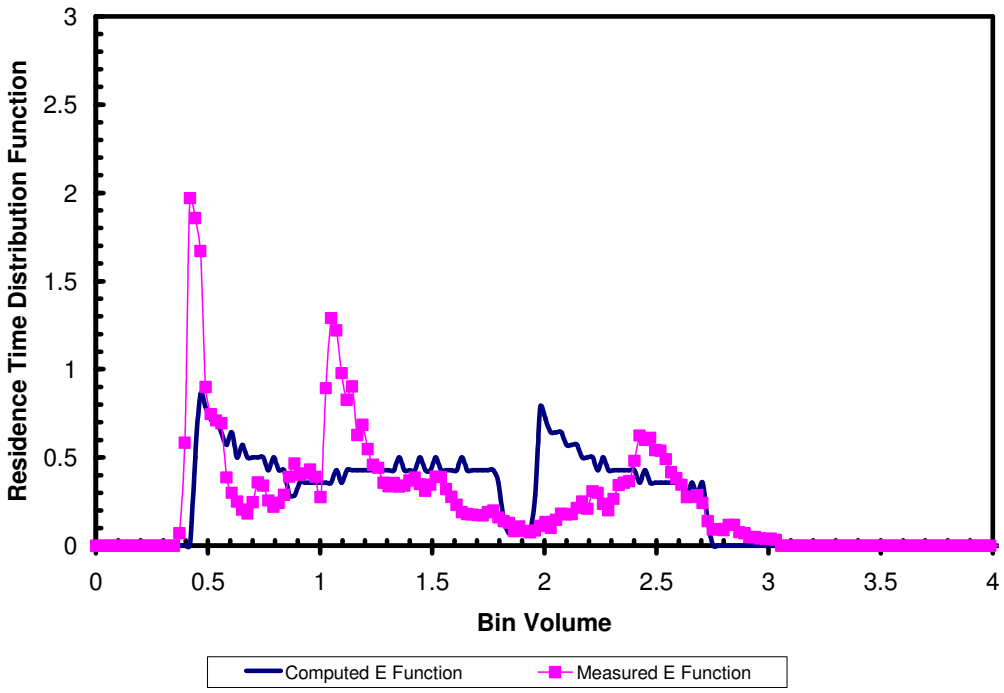

Figure 19. Computed and measured residence time distribution function for model bin

Blender effectiveness in the cone-in-cone blender depends on the velocity distribution across the blender. Therefore, anything that changes the velocity distribution will also change the blender effectiveness. Differences in wall friction angle change the velocity distribution and will result in changes to blender performance depending on the blender operation. However, Equations 13 and 14 also contain the effect of the local pressure gradient. These pressure gradient values can result in differences in velocity profiles in the cone-in-cone blender. Significant gas pressure gradients can affect mixing in cone-in-cone blenders when discharging fine powder materials. Gas pressure gradients arise from the fact that bulk materials are compressible and change porosity as solids contact stresses within the equipment change and are impermeable. For example, consider a bulk powder material flowing at a slow rate through a cone-in-cone blender. The solid's stresses increase as material flows through the bin. This causes some consolidation of the bulk material and squeezes some air out of the solid's pores. Gas leaves the system predominately through the top material free surface. However, the consolidation pressure in the bin or hopper decreases as the material approaches the outlet. Decreasing consolidation pressure results in expansion of the bulk material. However, some of the gas within the solid's pores has already left the system through the top of the bin. This results in a net gas deficit near the hopper outlet, creating negative gas pressures within the material and producing significant negative gas pressure gradients near the outlet. These gas pressure gradients could be responsible for changing the local velocity profiles in the bin. The cone-in-cone hopper situation is complicated by the fact that the inner cone wall is impervious to gas flow. Thus, there exists a difference in radial gas pressure gradients between the inner cone and the annular region in the cone-in-cone blender. This could significantly change the blender effectiveness of cone-in-cone blenders. Figures 20 and 21 show the expected gas pressure and gas pressure gradient profiles in both the inner cone and annular region for a typical cone-in-cone blender.

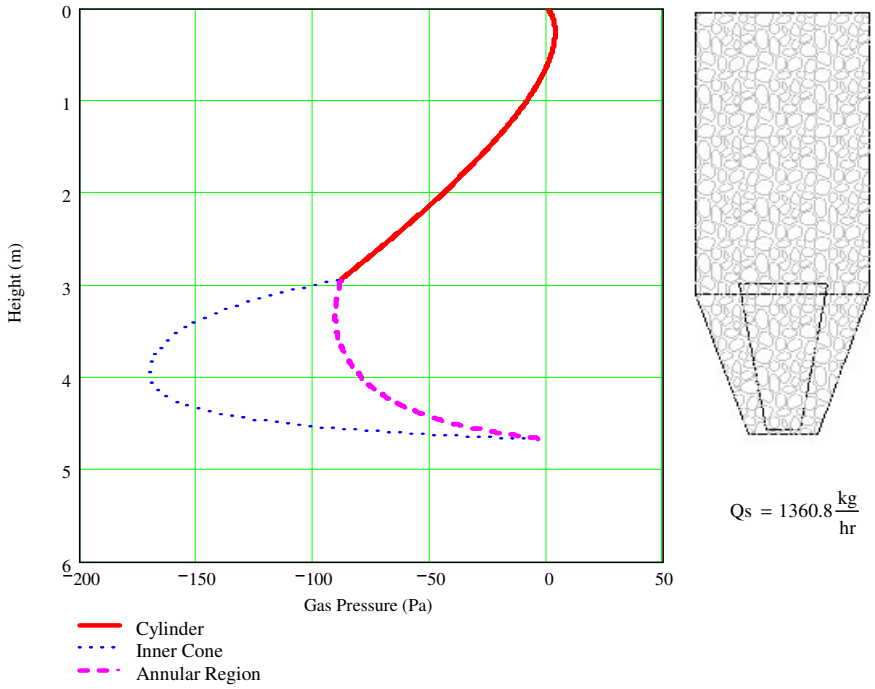

Figure 20. Gas pressure profile in cone-in-cone blender when operating with fine plastic powder at a flow rate of 1360.8 kg/hr (about 30% of the expected limiting flow rate for this powder). Velocity ratio between inner and outer cone is 2:1

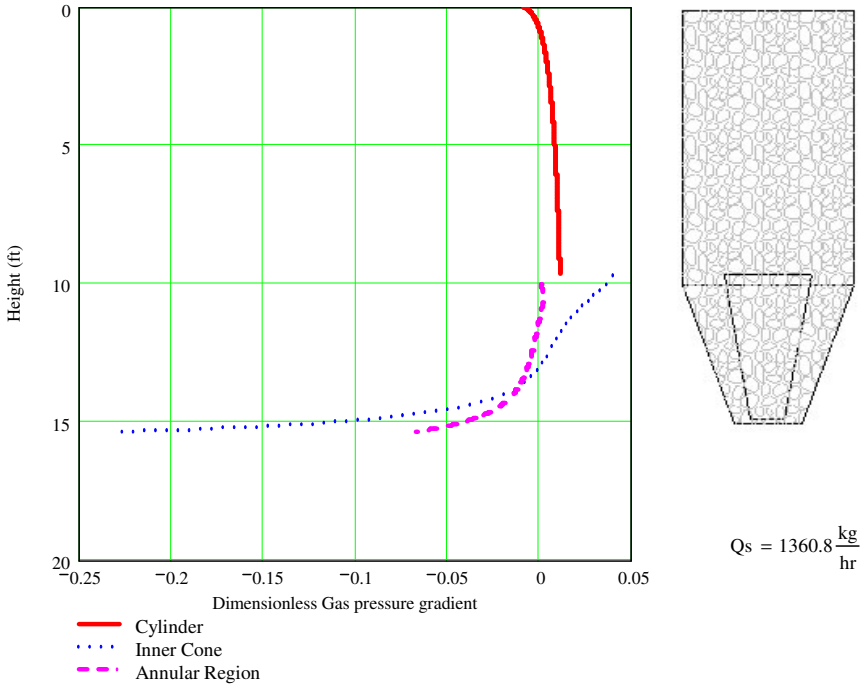

Figure 21. Radial gas pressure gradient (dP/dr / ρg) in cone-in-cone blender when operating with fine plastic powder at a flow rate of 1360.8 kg/hr (±30% of expected limiting flow rate for this powder). Velocity ratio between inner and outer cone is 2:1

Once the local gas pressure gradients are known, the radial velocity analysis outlined above can be implemented to compute the expected velocity profiles for the case of the local radial pressure gradients given in Figure 22. This analysis can be applied to both the inner cone and the annular region to determine the velocity profiles at various local gas pressure gradients. Figure 22 shows the expected velocity profiles in the 10 degree inner cone at different radial gas pressure gradients. Note that the negative gas pressure gradient at the bottom of the inner cone is large enough to result in a funnel-flow velocity pattern. If this high gas pressure gradient persisted throughout the inner cone section, it would induce a funnel flow velocity pattern in the blender and result in a preferred flow channel. Luckily the gradients in other hopper elevations are smaller than this value. Likewise, Figure 23 indicates that if gas pressure gradients in the annular section have large enough negative values, then preferred flow channels would develop along the outer wall of the inner cone. Each of the velocity profiles in these figures has been normalized so the velocity at the centerline equals one.

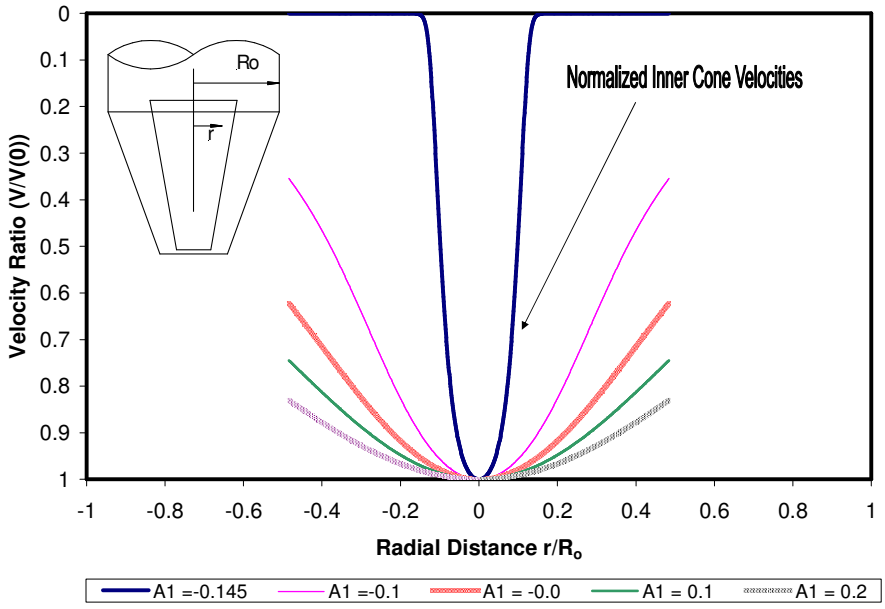

Figure 22. Normalized velocity profiles for inner cone at various local gas pressure gradients A1 = (dP/dr / γg)

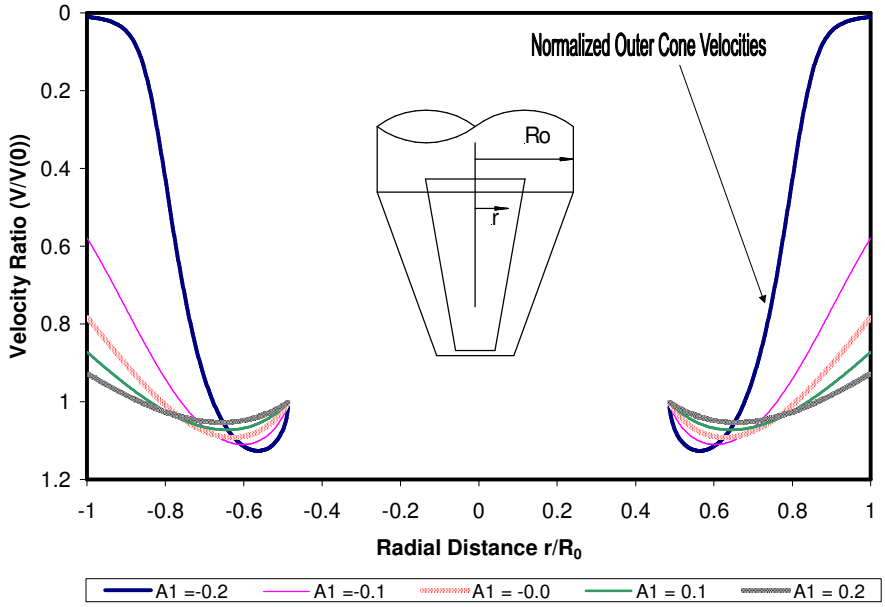

Figure 23. Normalized velocity profiles in annular section of cone-in-cone hopper as a function of local gas pressure gradient A1 = (dP/dr / γg)

However, local velocity profiles at any elevation in the blender can be computed by assuming a two-to-one velocity difference between the inner and outer cone and computing the velocity profile from the local gas pressure gradient given in Figure 20. Figure 24 shows several of these velocity profiles in the hopper section of the cone-in-cone blender. This figure indicates that the steep funnel flow velocity pattern persists only near the hopper outlet. Velocity profiles near the top of the cone section are actually flatter than those expected for normal mass flow without gas pressure effects. It is not likely that the small zone of steep velocity profiles near the inner hopper outlet will promote complete funnel-flow behavior in the entire hopper section. However, increasing the solids flow rate will increase the magnitude of these negative gas pressure gradients in the lower hopper and increase the positive gas pressure gradients in the upper hopper section. This suggests that one should expect to see a flow rate condition that may induce a preferred flow channel formation in the center of the blender during operation at high flow rates. Conversely, the higher gas pressure gradient at the top of the hopper would likely result in overall average velocity profiles flatter than typical velocities in mass flow blenders without gas pressure gradient effects. This suggests that the blending action of the blender may diminish as the flow rate of fine powder increases until the very steep profile in the lower hopper section occupies a significant portion of the bin, at which point the blender velocity profile produces funnel flow behavior. The whole matter of the influence of local gas pressure gradient in cone-in-cone blenders is an interesting area for further study. However, this theoretical analysis suggests that fine powders may be susceptible to preferred flow channel formation in cone-in-cone blenders if conditions are right.

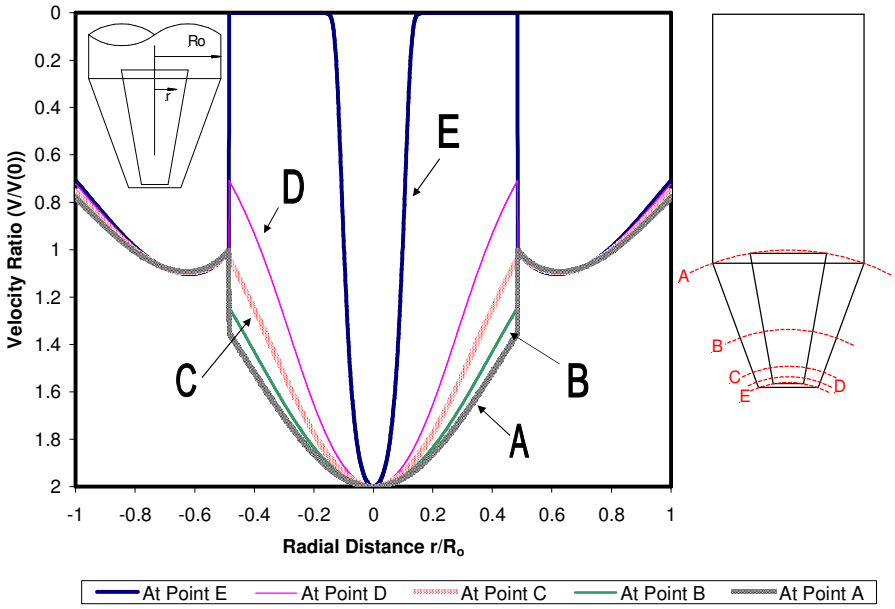

Figure 24. Velocity profiles in cone-in-cone blender at various locations in the blender. The mass flow rate in this blender is 1360.8 kg/hr with a two to one velocity ratio between the inner cone and the annular section.

Conclusions

The strength of this paper is the ability to compute the residence time distribution function just from knowledge of material properties. The properties induce a unique velocity pattern in a given cone-in-cone geometry that can be approximated using limiting states of stress in the blender. The radial velocity assumption allows radial velocity fields to be extended to annular flow channels. The analysis in this paper suggests that the blender design is somewhat independent of wall friction angle for conditions where there are several input concentration fluctuations in a single blender volume. However, friction angle does play a role in blender performance for conditions where the blender must mix large-period input fluctuations. Radial velocity profiles in cone-in-cone blenders can be extended to include the effect of local gas pressure gradients. There is some evidence that these gas pressure gradients can induce funnel-flow behavior in the blender, depending on the operation flow rate, and may result in preferred flow channels during operation. This is an area for further research. It is the contention of the author that the method of blender evaluation outlined above could be used with other blender configurations to develop a bridge between blender effectiveness and the material properties which control the velocity profiles in the blender. This general methodology, if successfully implemented, will allow scale-up of blenders. This will likely require solving complex 3D differential equations with free boundaries to obtain an approximation to the local velocity patterns. Even though this is a formidable task, the author suggests this road as the way forward. Advances in volume of fluid finite element methods or a combination of DEM and FEM approaches may provide the necessary computational power to accomplish this task.

Nomenclature

A_1	Dimensionless radial pressure gradient body force ratio
A_2	Dimensionless θ˜-direction pressure gradient body force ratio
BV	Bin volume
$Cap_{blender}$	Blender capacity
C_{in}	Input concentration
C_{out}	Output concentration
D_T	Top diameter of outer cone (m)
d_T	Top diameter of inner cone (m)
D_B	Bottom diameter of outer cone (m)
d_B	Top diameter of inner cone (m)
D_O	Outlet diameter of cone-in-cone hopper (m)
$E(t)$	Residence time distribution function $E(t) = dF(t)/dt$
$F(t)$	Cumulative residence time distribution function
P	Gas pressure (KPa)
Q_S	Solids flow rate (kg/hr)
r	Radial coordinate (m)
R_{vel}	Ratio of inner and outer velocities in cone-in-cone hopper
r_b	Distance from the hopper centerline to hopper radial coordinate (m)
R_b	Distance from the hopper centerline to the hopper wall (m)
s	θ-dependence function for radial stress
$Sdev_{in}$	Standard deviation of input stream
$Sdev_{out}$	Standard deviation of output stream
$V(\theta)$	Radial velocity (m/s)
$V(0)$	Velocity at hopper centerline (m/s)
$V(r_b)$	Radial velocity in terms of distance from centerline (m/s)
V_{center}	Velocity at hopper centerline (m/s)
VR	Variance reduction factor
γ	Powder bulk density (kg/m^3)
β	Angle between effective wall body force and gravitational vector direction (deg)
δ	Effective internal friction angle (deg)
φ_w	Wall friction angle (deg)
φ_{we}	Effective wall friction angle including gas pressure gradient terms (deg)
σ_r	Normal stress on the plane perpendicular to the radial direction in a spherical coordinate system (KPa)
σ_θ	Normal stress on the plane perpendicular to the θ-direction in a spherical coordinate system (KPa)
σ_φ	Normal stress on the plane perpendicular to the φ-direction in a spherical coordinate system (KPa)
σ	Mean stress (KPa)
σ_1	Major principal stress (KPa)
σ_3	Minor principal stress (KPa)
θ_w	Half angle of conical hopper measured from the vertical (deg)
θ_i	Half angle of inner conical hopper measured from the vertical (deg)
θ_o	Half angle of outer conical hopper measured from the vertical (deg)

θ_L	Half angle of conical hopper at bottom of cone-in-cone (deg)
θ	θ-direction coordinate (deg)
φ	φ-direction coordinate (deg)
φ_w	Wall friction angle (deg)
φ_{we}	Effective wall friction angle (deg)
$\tau_{r\varphi}$	Shear stress on the plane perpendicular to the radial direction acting in the φ-direction in a cylindrical coordinate system (KPa)
$\tau_{r\theta}$	Shear stress on the plane perpendicular to the radial direction acting in the θ-direction in a cylindrical coordinate system (KPa)
$\tau_{\theta\varphi}$	Shear stress on the plane perpendicular to the θ-direction acting in the φ-direction in a cylindrical coordinate system (KPa)
ω	Angle between the major principal stress and the r-coordinate direction (KPa)

Acknowledgment

The author would also like to acknowledge the financial support of the Engineering Research Center (PERC) for Particle Science and Technology at the University of Florida, Material Flow Solutions Inc, the National Science Foundation NSF Grant #EEC-94-02989, and the Industrial Partners of the PERC.

References

1. BMHB, Silos: *Draft Design Code for Silos, Bin, Bunkers and Hoppers* (1987)
2. Ebert, F., Dau, G., and Durr, V., *Blending Performance of Cone-in-Cone Blenders – Experimental Results and Theoretical Predictions*, Proceedings of The 4th International Conference for Conveying and Handling of Particulate Solids (2003)
3. Johanson, J.R., *Controlling Flow Patterns in Bins by Use of an Insert*, Bulk Solids Handling, V2, N3 Sept (1982)
4. Jenike, A.W., Johanson J.R., *Stress and Velocity Fields in Gravity Flow of Bulk Solids, Bulletin 116*, Utah Engineering Station (1967)
5. Nedderman, R.M., *Statics and Kinematics of Granular Materials*, Cambridge University Press, (1992)
6. Sokolovskii, V.V., *Statics of Granular Media*, Pergamon Press, Oxford (1965)
7. Jenike, A.W., *Gravity Flow of Bulk Solids, Bulletin 108*, Utah Engineering Station (1961)
8. Jenike, A.W., *Flow and Storage of Bulk Solids, Bulletin 123*, Utah Engineering Station (1967)
9. Jenike, A.W., Powder Technology, V50, p229 (1987)